Article

Magnetotactic Bacteria AMB-1 with Active Deep Tumor Penetrability for NIR-II Photothermal Tumor Therapy

Guoming Huang, Guifen Zhu, Ruipeng Lin, Wenwen Chen, Rong Chen, Yutong Sun, Liqun Chen,* Dengke Hong,* and Lihong Chen*

Read Online

ACCESS | Metrics & More | Article Recommendations | Supporting Information

ABSTRACT: The complex tumor structure and microenvironment such as abnormal tumor vasculature, dense tumor matrix, and elevated interstitial fluid pressure greatly hinder the penetration and retention of therapeutic agents in solid tumors. The development of an advanced method for robust penetration and retention of therapeutic agents in tumors is of great significance for efficient tumor treatments. In this work, we demonstrated that magnetotactic bacteria AMB-1 with hypoxic metabolism characteristics can actively penetrate the tumor to selectively colonize deep hypoxic regions, which emerge as a promising intelligent drug carrier. Furthermore, AMB-1 presents intrinsic second near-infrared (NIR-II) photothermal performance that can efficiently convert a 1064 nm laser into heat for tumor thermal ablation. We believe that our investigations not only develop a novel bacteria-based photothermal agent but also provide useful insights for the development of advanced tumor microbial therapies.
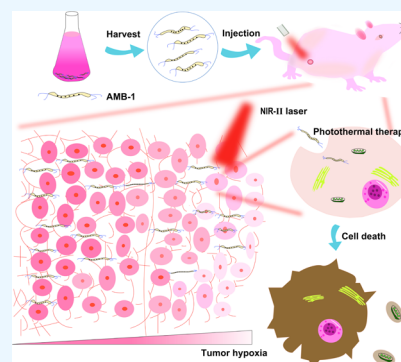
1. INTRODUCTION

Photothermal therapy (PTT) is considered a promising cancer treatment strategy, which kills tumor cells through irreversible cell damage caused by heat-induced protein denaturation or cell membrane destruction.[1,2] In recent years, this therapeutic method has become a hotspot in tumor treatment research because of its advantages of high specificity, noninvasiveness, easy operation, and low cost. A variety of nanomaterials, such as noble metal (gold, silver, platinum, palladium) nanomaterials, carbon nanomaterials, transition-metal chalcogenides, and organic nanomaterials, have been extensively developed as photothermal agents, which can absorb light to generate photothermal effects.[3−7] Despite the significant progress in the development of novel photothermal agents, the penetration and retention of photothermal agents in tumors, especially solid tumors, still face great challenges due to the complex structure and microenvironment of tumors.

The biological challenges that obstruct the penetration and retention of photothermal agents in tumors mainly include abnormal tumor vasculature, dense tumor matrix, and elevated interstitial fluid pressure (IFP).[8−10] Tumor blood vessels are generally more permeable and more heterogeneous in distribution than normal vasculature.[11] Although the leakiness of tumor blood vessels is beneficial for the extravasation of therapeutic agents, it damages the perfusion function of the vasculature.[12] Moreover, the rapid proliferation of tumor cells reduces the density of blood vessels and leads to heterogeneity in the distribution of blood vessels, forming areas (e.g., hypoxic areas) where therapeutic agents are difficult to perfuse.[13] The extracellular matrix of solid tumors is composed of various

components such as collagens, elastin, glycoproteins, and proteoglycans.[14] These matrix components cross-link with each other to form a complex and dense network structure accompanied by progressive tissue stiffening, which greatly hinders the penetration of therapeutic agents throughout a solid tumor.[15] In addition, because of the lack of a lymphatic system, solid tumors usually present a much higher IFP than that of normal tissues.[13,16] The elevated IFP induces an outward net convection flow in the tumor interstitium, restricting the intratumoral transport and retention of therapeutic agents in tumors.[13,16] These biological barriers not only hinder the entry of therapeutic agents into tumors but also cause the rapid clearance of therapeutic agents from tumors, significantly limiting the concentration and action time of therapeutic agents in tumors.

The specific structure and microenvironment of tumors generate great biological barriers to tumor treatment, but they also provide opportunities for the development of advanced cancer therapies. For example, anaerobic bacteria have been shown to selectively colonize deep tumor hypoxic areas due to their hypoxic metabolism properties and the pathophysiological features of solid tumors, which have emerged as promising carriers for delivering therapeutic payloads.[17−19]

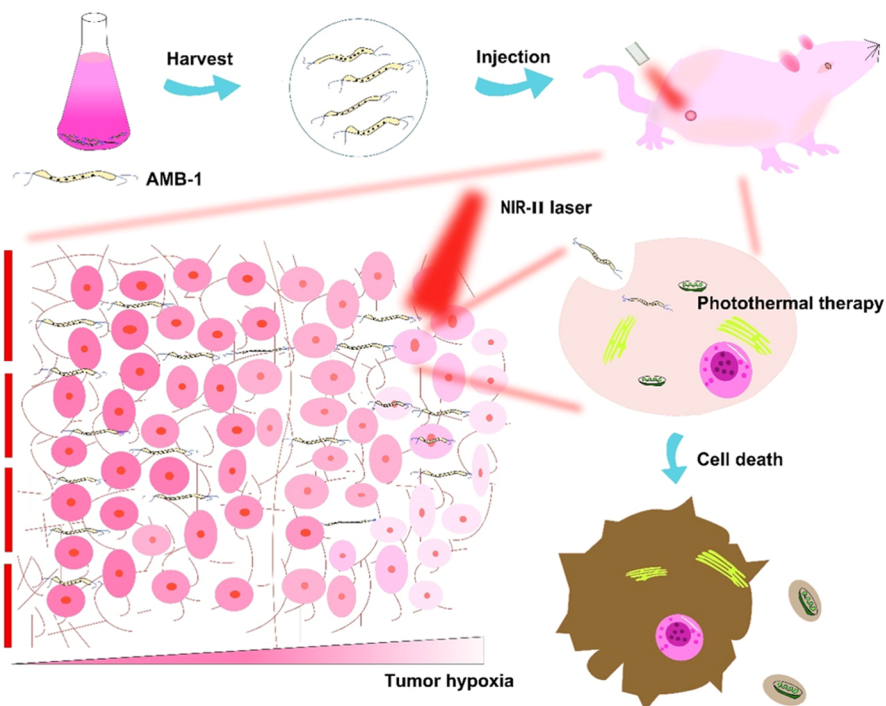**Scheme 1. Schematic Illustration of Magnetotactic Bacteria AMB-1 for NIR-II Photothermal Tumor Therapy**

Hypoxia is a typical characteristic of most solid tumors.[20−22] The hypoxic tumor regions provide a suitable environment for the anaerobic growth of anaerobes. In addition, a large number of metabolites produced by the rapid proliferation of tumor cells can be utilized by anaerobic bacteria, which is also beneficial for bacterial growth. Furthermore, the immune-suppressive microenvironment of tumors leads to a much slower immune clearance of bacteria in tumors than in normal tissues.

Recently, several bacteria such as *Escherichia coli* and *Salmonella typhimurium* have been developed as versatile carriers for delivering photothermal agents.[23−30] However, these strategies typically involve the covalent coupling of bacteria and photothermal agents or *in situ* synthesis of photothermal agents on bacterial surfaces, which are complex and tedious. Magnetotactic bacteria are a type of facultative anaerobe, which contain a specialized organelle called magnetosome.[31] Magnetosomes are mainly composed of lipid bilayer membrane-enveloped magnetic nanoparticles (Fe_3O_4 or Fe_3S_4).[32] Because of the excellent magnetic properties of magnetosomes, magnetotactic bacteria have been applied in magnetic biomedicine such as magnetic hyperthermia and magnetomechanical therapy.[33−35] However, the intrinsic photothermal performance of magnetotactic bacteria still lacks investigation. In this work, we studied the intrinsic photothermal effect and tumor penetrability of magnetotactic bacteria AMB-1. We found that *Magneto-spirillum magneticum* AMB-1 presents excellent second near-infrared (NIR-II) photothermal performance that can effectively convert NIR-II excitation light into heat. NIR-II excitation lights have higher tissue penetration depth than ultraviolet−visible and NIR-I lights due to their lower absorption and scattering of photons by tissues.[36] Moreover, AMB-1 exhibits tumor hypoxia targeting ability that can deeply penetrate the tumor and selectively colonize hypoxic regions. AMB-1, with high photothermal conversion property and

robust tumor colonization, thus holds great promise for efficient thermal ablation of solid tumors (Scheme 1).

2. EXPERIMENTAL SECTION

2.1. Culture of AMB-1. *M. magneticum* AMB-1 was purchased from the American Type Culture Collection (ATCC700264). The resuscitated AMB-1 bacteria were added to 1 L of magnetic spirillum growth medium (MSGM) in a 2.5% ratio. The bacteria culture was carried out in a shaker at 50 rpm and 26 °C for 5−7 days under an anaerobic condition. The as-cultured AMB-1 bacteria were harvested by centrifugation at 9000 rpm at 4 °C for 5 min. Finally, the bacteria were resuspended in a phosphate-buffered saline (PBS) solution for further use.

2.2. Characterization. Scanning electron microscopy (SEM) images were collected on a Nova NanoSEM 230 microscope. The bacteria were fixed by 2.5% glutaraldehyde for SEM. Transmission electron microscopy (TEM) images were obtained using a Hitachi HT7700 microscope at 100 kV. High-resolution TEM and energy-dispersive X-ray (EDX) elemental mapping images were collected on a Tecnai G2 F20 microscope at 200 kV. The absorption spectrum was measured using a Hitachi UH4150 UV−visible−near-infrared (UV−visible−NIR) spectrophotometer. Iron content in the bacteria was detected by XSeries 2 inductively coupled plasma mass spectrometry (ICP-MS).

2.3. Investigations of Photothermal Performance. To assess the photothermal performance of AMB-1, 200 μL of the AMB-1 suspension (400 μg mL^{-1}) was added to a 96-well plate. Then, the AMB-1 suspension was treated with laser irradiation of different wavelengths (660, 808, and 1064 nm) at different power densities (0.6, 0.8, 1.0, 1.2, and 1.4 W cm^{-2}) for 10 min. The temperature of the suspension was recorded by a thermocouple. Moreover, AMB-1 suspensions of different concentrations (200, 300, 400, 500, and 600 μg mL^{-1}) were prepared, and the power density was set at 1.2 W cm^{-2} to

evaluate the photothermal performance of AMB-1 under different concentrations.

To investigate the tissue penetration depth of laser of different wavelengths (660, 808, and 1064 nm), pork with different thicknesses (2, 5, 7, 10, 15, and 20 mm) was prepared. The AMB-1 suspension (200 μL, 400 μg mL^{-1}) was added to a 96-well plate, and the suspension was covered with pork tissues during the laser irradiation (1.2 W cm^{-2}, 3 min). The temperature changes of the suspension were recorded to obtain the temperature decay curves.

For infrared thermal imaging, 1 mL of the AMB-1 suspension (400 μg mL^{-1}) was added to an EP tube and then irradiated with a 1064 nm laser at 1.2 W cm^{-2}. Thermal images were collected by an FLIR Ax5 infrared camera at different time points (0, 2, 4, 6, 8, and 10 min), and PBS was used as control.

To investigate the photothermal stability of AMB-1, the AMB-1 suspension (200 μL, 400 μg mL^{-1}) was added to a 96-well plate and then irradiated with a 1064 nm laser at 1.2 W cm^{-2} for 10 min. Then, the laser was turned off, and the suspension was cooled for 10 min. This laser on/off cycle was repeated four times continuously, and the temperature change over the entire process was recorded.

The photothermal conversion efficiency of AMB-1 was calculated according to the following formula: $\eta = (hA\Delta T_{max} - Q_s)/I(1 - 10^{-A})$, where h is the heat transfer coefficient, A is the surface area of the container, ΔT_{max} is the temperature change at maximum steady-state temperature, Q_s is the heat dissipation from the light absorbance of the solvent and container, which is independently measured using quartz cell containing pure water, I is the laser power density, and A is the absorbance of AMB-1 at 1064 nm. The value of hA can be determined by the following formula: $\tau_s = (m_D C_D)/hA$, where τ_s is the system time constant, which can be obtained by the slope of the plot of cooling time versus $-\ln(\Delta T/\Delta T_{max})$, and m_D and C_D are the mass and heat capacities of water, respectively.

2.4. In Vitro Photothermal Therapy. The photothermal cytotoxicity of AMB-1 was evaluated by a standard Cell Counting Kit-8 (CCK-8) assay. MCF-7, Walker 256, and L02 cells were seeded into 24-well plates with a transwell. MCF-7 and L02 cells were cultured with the RPMI-1640 medium, while Walker 256 cells were cultured with the DMEM medium. The cells were incubated in a 5% CO_2 atmosphere at 37 °C for 24 h. Then, the cells were incubated with AMB-1 of different concentrations for 30 min. Subsequently, the cells were irradiated with a 1064 nm laser at 1.2 W cm^{-2} for 3 min. After another 2 h of incubation, the transwells containing AMB-1 were removed, and the medium was discarded. The cells were washed with PBS three times. Then, the medium containing 10% CCK-8 was added to the cells for further incubation (0.5−4 h). Finally, the absorbance of the samples at 450 nm was measured with a microplate reader (SH-1000 Lab).

For Calcein-AM/PI co-staining or JC-1 staining, MCF-7 cells were seeded into 35 mm Petri dishes and cultured with the RPMI-1640 medium at 37 °C in a humidified 5% CO_2 atmosphere for 24 h. Subsequently, 400 μg mL^{-1} of AMB-1 was added. After incubation for another 4 h, the cells were washed with PBS 3 times. For the AMB-1 + laser group, the cells were then irradiated with a 1064 nm laser (1.2 W cm^{-2}) for 6 min and further incubated for another 2 h. Afterward, the cells were stained with Calcein-AM and PI solutions (4 μM) or

JC-1 according to the kit procedure. Finally, the cells were imagined by an inverted fluorescence microscope system or confocal laser scanning microscope.

2.5. Magnetic Resonance Imaging. T_2-weighted phantom imaging and transverse relaxivity measurements were performed on a 0.5 T NMR120-Analyst NMR system (Niumag, Shanghai). A 1% agarose containing AMB-1 with different Fe concentrations was prepared. T_2-weighted images were collected by a two-dimensional (2D) MSE sequence by using the following parameters: TR = 2000 ms, TE = 40 ms, thickness = 1 mm, slice = 1, 512 × 512 matrices, and NS = 4. The transverse relaxation time (T_2) was measured by a CPMG sequence.

In vivo T_2-weighted imaging was performed by a 3T GE discovery 750 W MRI. To construct a subcutaneous tumor model, MCF-7 cells (1 × 10^6 cells) were subcutaneously injected into the right limb of male BALB/c nude mice. When the tumor volume reached about 80 mm^3, T_2-weighted images of the mice with and without the injection of AMB-1 suspension (100 μL, 400 μg mL^{-1}) were collected using an FSE-T2WI sequence (TR = 4500 ms; TE = 82 ms; thickness = 2 mm). All animal experiments in this work were performed in accordance with the Guide for the Care and Use of Laboratory Animals (Ministry of Science and Technology of China, 2006) and were approved by the Institutional Animal Care and Use Committee of Fuzhou University.

2.6. Tumor Penetrability of AMB-1. The hypoxic staining was performed according to the protocol of the Hypoxyprobe-1 plus kit. MCF-7 tumor-bearing nude mice were peritumorally injected with 100 μL of an AMB-1 suspension. After 24 h, 100 μL of Hypoxyprobe-1 (hypoxia marker) was intraperitoneally injected into the tumor-bearing mice. Then, the tumor was excised after 0.5−1 h, and the sections at 2, 5, and 7 mm away from the injection point were prepared. Mouse FITC-conjugated mouse monoclonal antibody antipimonidazole was added to the tumor sections overnight at 4 °C. Then, a secondary anti-FITC horseradish peroxidase (HRP) antibody was added for 30 min. DAB color development was subsequently carried out, and hematoxylin counterstaining (45 s) was finally performed. For AMB-1 bacteria staining, a similar procedure was employed except that the primary and secondary antibodies are TLR4/Toll-like receptor 4 rabbit polyclonal antibody and HRP-labeled goat antirabbit IgG (H + L) antibody, respectively.

2.7. In Vivo Photothermal Therapy. The MCF-7 tumor-bearing BALB/c nude mice were randomly divided into three groups. In the blank group, the mice were without any treatment. In the laser group, the mice were irradiated with a 1064 nm laser (1.2 W cm^{-2}, 5 min). In the AMB-1 + laser group, the mice were injected with AMB-1 (100 μL, 400 μg mL^{-1}) and then irradiated with a 1064 nm laser (1.2 W cm^{-2}, 5 min). To observe the in vivo photothermal conversion performance of AMB-1, an infrared thermograph (FLIR Ax5) was used to collect thermal images of tumor sites under a 1064 nm laser irradiation. The tumor length and width were recorded by a vernier caliper during the treatments to monitor the tumor growth. Relative tumor volume is defined as V/V_0, where V is the tumor volume (V = length × width^2/2) and V_0 is the initial tumor volume. In addition, the body weights of the mice were also recorded during the treatments.

2.8. H&E and TUNEL Staining. To examine the damage to tumor tissue after the treatments, the mice were executed and the tumors were excised to prepare tissue sections after 24
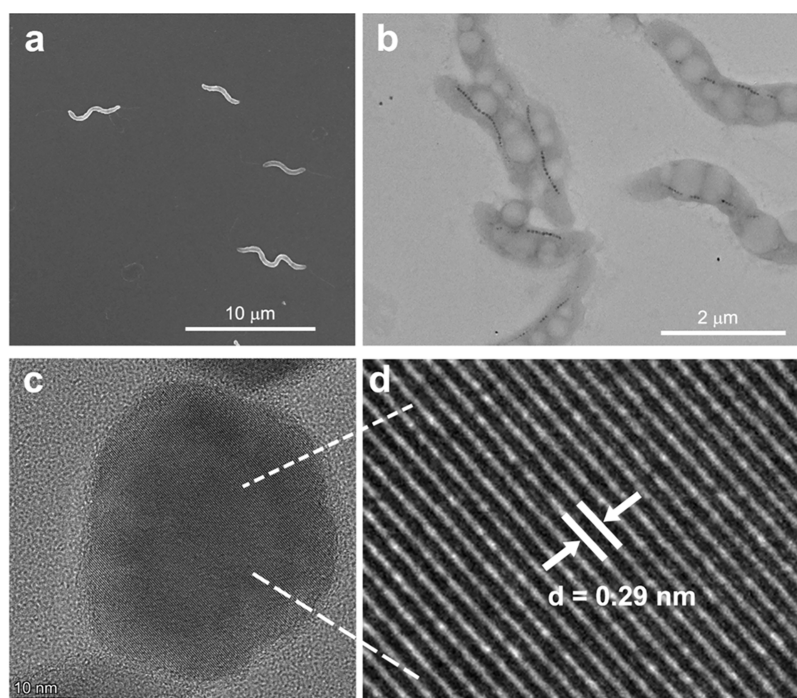
Figure 1. (a) SEM and (b) TEM images of AMB-1. (c) HRTEM images of magnetosome.

h. Then, the H&E and TUNEL staining for tumor sections was carried out according to the standard protocols. Ten days after the treatments, major organs of the mice including the heart, liver, spleen, lung, and kidney were also excised to prepare H&E-stained tissue sections for investigating the safety of the AMB-1-mediated NIR-II photothermal treatment. To evaluate the acute systemic toxicity of AMB-1, the mice were sacrificed 24 h after the intravenous injection of AMB-1 (100 μL, 400 μg mL^{-1}), and heart, liver, spleen, lung, and kidney of the mice were collected for H&E staining.

2.9. Hemolysis Assay. Blood was sampled from BALB/c nude mouse eyes, and red blood cells (RBCs) were collected by centrifugation (2000 rpm, 10 min). The collected RBCs were washed with PBS until the supernatant was transparent and clear. To investigate the hemolysis effect of AMB-1, 0.5 mL of AMB-1 suspensions with different concentrations was added to 0.5 mL of a 4% RBC solution. The mixtures were centrifuged after incubation for 4 h. Moreover, 100 μL of the supernatants was added to a 96-well plate, and the absorbance at 540 nm (A_{sample}) was measured by a microplate reader for calculating the hemolysis rate: hemolysis rate (%) = (A_{sample} − $A_{negative}$)/($A_{positive}$ − $A_{negative}$) × 100%, where $A_{positive}$ and $A_{negative}$ are the absorbances of negative control (PBS) and positive control (H$_2$O), respectively.

3. RESULTS AND DISCUSSION

We cultured AMB-1 in a magnetic spirillum growth medium (MSGM) under microaerobic conditions. Scanning electron microscopy (SEM) and transmission electron microscopy (TEM) were used to observe the morphology of the as-cultured AMB-1. SEM image shows that AMB-1 exhibits a helical shape with a bacterial length of 3−4 μm, and the flagella can be clearly observed (Figure 1a). The unique magnetosomes are further revealed by TEM (Figure 1b). They have an average particle size of 44.94 ± 6.78 nm and are arranged in a chain-like manner. TEM-associated energy-dispersive X-ray

(EDX) elemental mapping indicates that magnetosomes contain iron and oxygen elements (Figure S1). High-resolution TEM (HRTEM) image reveals that the lattice spacing of the magnetosome core is about 0.29 nm, which corresponds to the (220) crystal plane of Fe$_3$O$_4$ (Figure 1c). These results suggest that we have successfully cultivated magnetotactic bacteria AMB-1 containing rich magnetosomes.

We then studied the photothermal performance of AMB-1. We first measured the absorbance spectrum of AMB-1. AMB-1 presents a broad absorbance from the visible region to the NIR region, indicating that AMB-1 has the potential for photothermal conversion (Figure 2a). We further investigated the photothermal properties of AMB-1 under the irradiation of lasers with different wavelengths, including 660 nm (visible), 808 nm (NIR-I), and 1064 nm (NIR-II). The AMB-1 suspension can effectively heat up under the irradiation of all lasers at different power densities (Figure S2). Notably, AMB-1 shows a much better heating performance under 1064 nm laser irradiation than other lasers. The photothermal heating effect of AMB-1 at different concentrations was also measured. AMB-1 exhibits concentration dependence, wherein the temperature of the AMB-1 suspension increases with the increase in concentration (Figure S3). Moreover, the best photothermal performance of AMB-1 under 1064 nm laser irradiation was confirmed again. The tissue penetrability of the excitation light source is an important consideration factor for the application of photothermal therapy. NIR-II lights usually present more deeper tissue penetration depths than visible and NIR-I lights because of its low scattering and absorption by biological tissues.[36] To investigate the tissue penetration depth of a laser of different wavelengths, we used pork with different thicknesses as model biological tissues (Figure S4). Fitted temperature decay curves reveal that the temperature decay rate under 1064 nm laser irradiation is much slower than that under 660 and 808 nm laser irradiation (Figure 2b), suggesting that 1064 nm laser has higher tissue penetrability to induce the
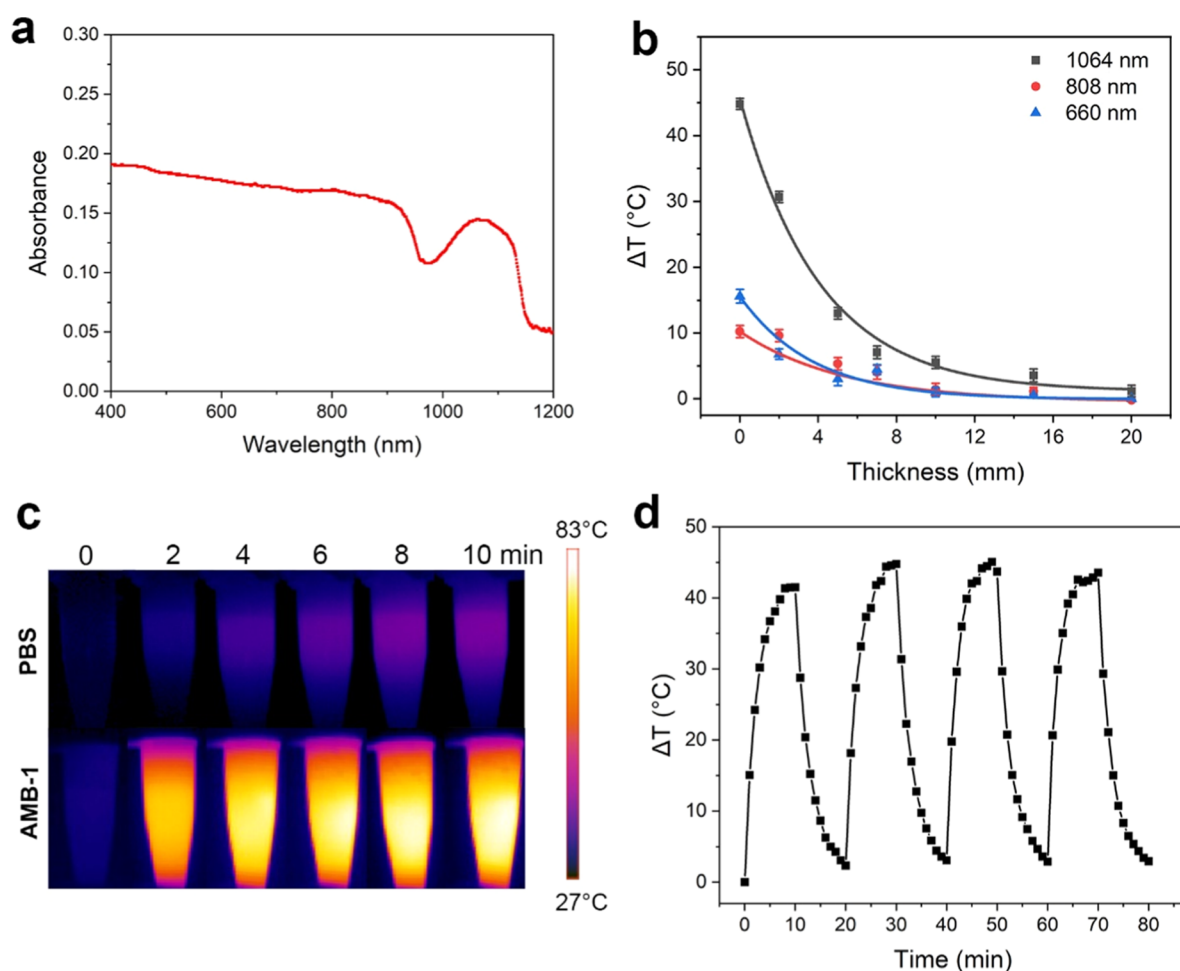
Figure 2. (a) Absorption spectra of AMB-1 suspension. (b) Fitted temperature decay curves of AMB-1 suspension under different laser irradiations with the covering of pork of different thicknesses. (c) Infrared thermal images of PBS and AMB-1 suspension under 1064 nm laser irradiation at different time points. (d) Photothermal stability testing curves of the AMB-1 suspension.

photothermal effects of AMB-1. Since the 1064 nm laser has deeper tissue penetration depth and can more efficiently induce the photothermal effects of AMB-1, we, therefore, used a 1064 nm laser as the light source for subsequent studies. To visually observe the photothermal properties of AMB-1 under a 1064 nm laser irradiation, we performed infrared thermal imaging (Figure 2c). The temperature of the AMB-1 suspension can rapidly increase to 70 °C within 10 min at the power density of 1.2 W cm^{-2}. In contrast, the temperature of PBS increases only to 35.1 °C. Moreover, the photothermal conversion efficiency (η) of AMB-1 is measured to be 41.56% (Figure S5). These results confirm that AMB-1 has excellent photothermal conversion performance that can effectively convert NIR-II light energy into thermal energy with high efficiency. The photothermal stability of AMB-1 was further tested. The heating performance of AMB-1 remains stable without a significant decrease after four cycles, suggesting the high photothermal stability of AMB-1 (Figure 2d).

Encouraged by the excellent photothermal conversion performance of AMB-1, we further studied the *in vitro* therapeutic effect of AMB-1 for photothermal inhibition of cancer cell growth. We first tested the cytotoxicity of AMB-1 on MCF-7, Walker 256, and L02 cells by the cell counting kit-8 (CCK-8) assay. No significant cytotoxicity is detected for all chosen cells without 1064 nm laser irradiation (Figure 3a). However, when the cells are exposed to a 1064 nm laser (1.2

W cm^{-2}, 3 min), the cell viabilities rapidly decrease with the increase of AMB-1 concentrations, indicating that the AMB-1-induced photothermal effect can effectively cause cell death. The cytotoxicity of AMB-1 was also verified by Calcein-AM and propidium iodide (PI) co-stained imaging (Figure 3b). Inverted fluorescence microscope images show that strong green Calcein-AM fluorescence was observed in the blank, laser-only, and AMB-1-only groups, revealing that MCF-7 cells in these control groups had no significant damage. Bright red PI fluorescence largely appeared in AMB-1 + laser groups, indicating that MCF-7 cells are severely damaged by AMB-1-induced photothermal effects. In addition, the damage mechanism of AMB-1 on MCF-7 cancer cells was investigated by the JC-1 mitochondrial membrane potential (MMP) assay. JC-1 was used as a fluorescence probe to detect the changes in MMP. MCF-7 cells in control groups mainly exhibit red fluorescence, suggesting that MMP in these cells has no significant changes (Figure 3c). In contrast, the cells display a large amount of green fluorescence after treatment with AMB-1 and 1064 nm laser irradiation, indicating the decrease of MMP due to the occurrence of early apoptosis. These results confirm that AMB-1 can effectively generate heat under 1064 nm irradiation to induce cell apoptosis for killing cancer cells.

Since the magnetosome of AMB-1 is mainly composed of Fe$_3$O$_4$, which is a typical magnetic nanoparticle, we further investigated the MRI performance of AMB-1. T_2-weighted
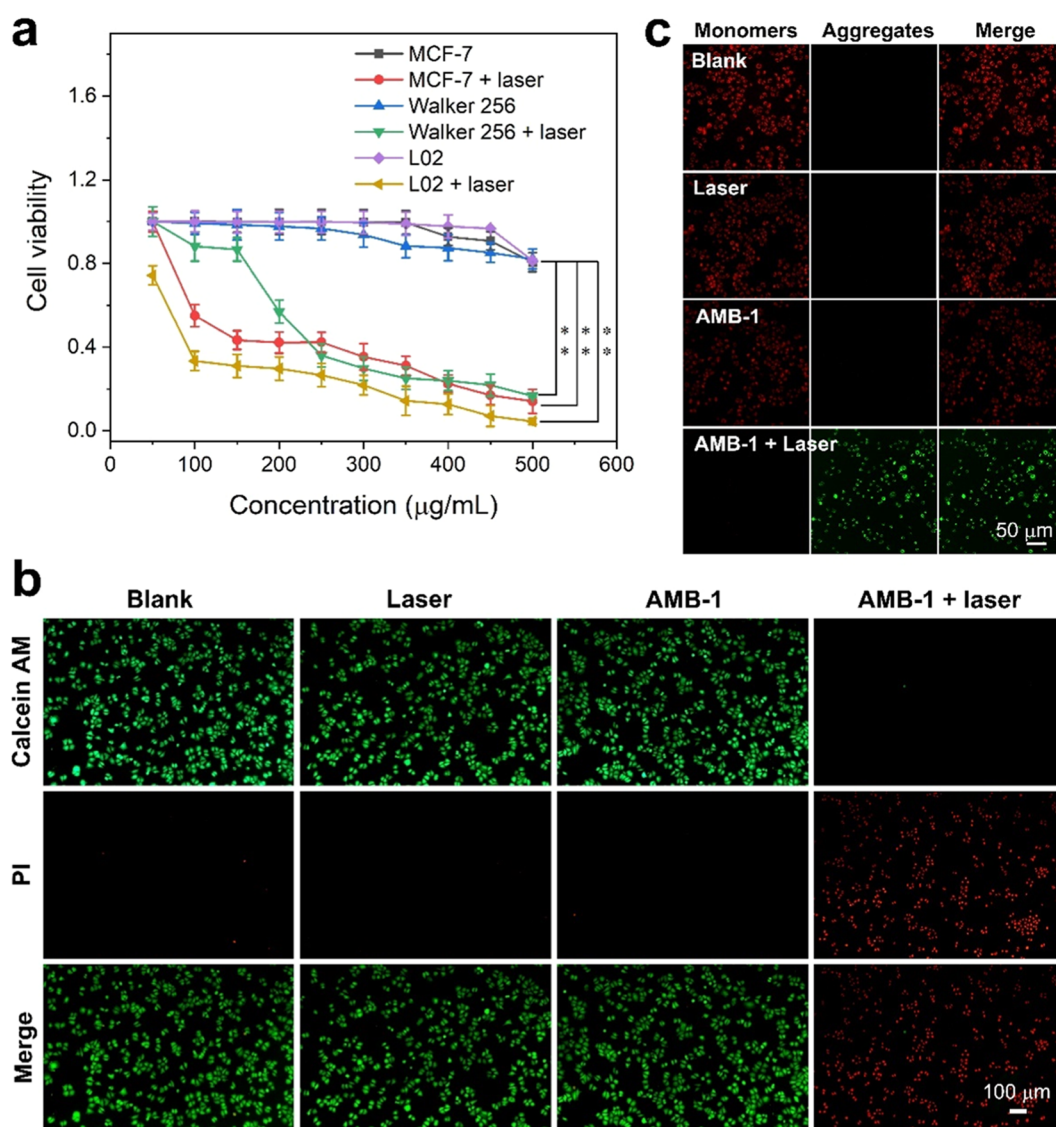
Figure 3. (a) Cell viabilities of MCF-7, Walker 256, and L02 cells after incubation of AMB-1 with or without 1064 nm laser irradiation (**P < 0.01). (b) Calcein-AM and PI co-stained and (c) JC-1-stained fluorescence images of MCF-7 cells with different treatments.

phantom imaging shows that the contrast signals become darker with the increase of iron concentrations, demonstrating the T_2 contrast enhancement performance of AMB-1 (Figure 4a). Moreover, the T_2 relaxation time of AMB-1 with various iron concentrations was measured, and the transverse relaxivity (r_2) was determined to be 223.08 ± 0.88 mM^{-1} s^{-1}, further confirming that AMB-1 can effectively shorten the T_2 relaxation time of water protons to generate T_2 contrast enhancement (Figure 4b). We then evaluated the *in vivo* MRI capability of AMB-1 using MCF-7 tumor-bearing nude mice as models. T_2-weighted images indicate that a significant negative contrast enhancement at the tumor site is observed after the injection of AMB-1, confirming that AMB-1 can also generate a T_2 relaxation shortening effect in tumor tissues for *in vivo* MRI contrast enhancement (Figure 4c). These results suggest that AMB-1 has the potential as an effective MRI contrast agent for imaging-guided photothermal therapy.
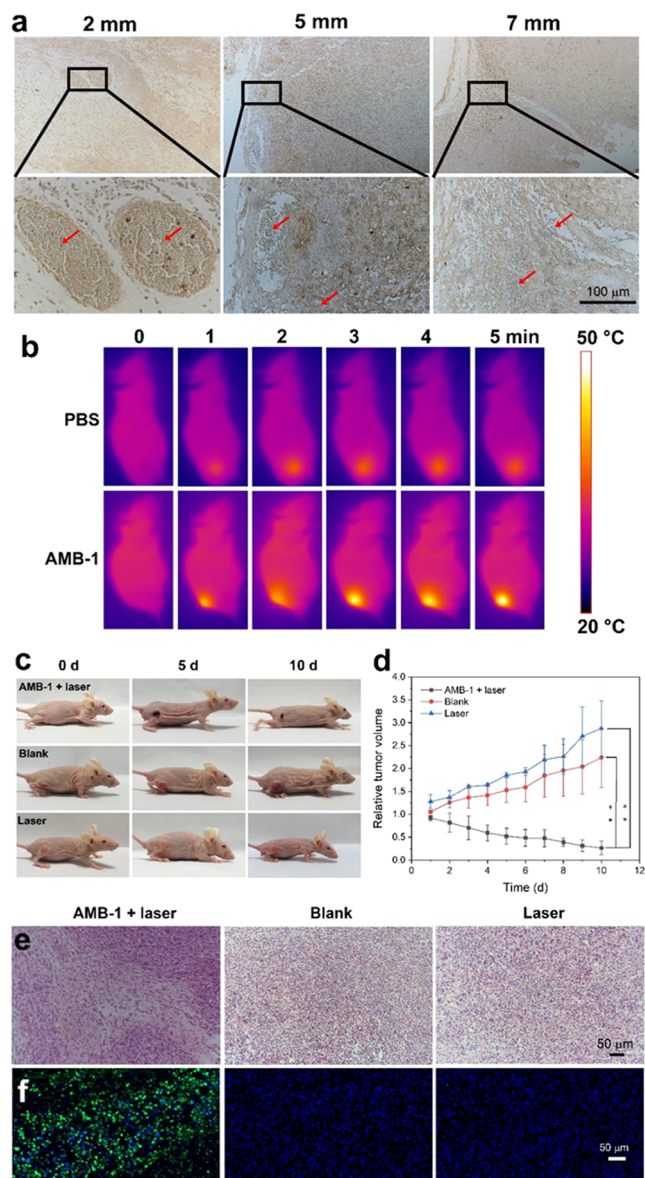
The penetration and retention of photothermal agents in solid tumors are of great importance for their therapeutic effectiveness. We, therefore, studied the tumor penetrability and tumor hypoxia-colonizing ability of AMB-1. AMB-1 was

peritumorally injected into a tumor-bearing nude mouse. After 24 h, the tumor was excised, and tumor tissue sections at 2, 5, and 7 mm away from the injection point were prepared for analysis. The hypoxic tumor regions were stained in brown by a hypoxia-specific probe, and the bacteria were stained with a lipopolysaccharide-specific probe. As shown in Figure 5a, AMB-1 (in blue, red arrows) can be observed in hypoxic regions in all tumor sections after the injection, indicating that AMB-1 can actively penetrate the tumor and selectively colonize hypoxic areas (Figure 5a). We then evaluated the *in vivo* photothermal therapy effect of AMB-1. To examine the *in vivo* photothermal conversion performance of AMB-1, we used an infrared thermograph to monitor the temperature changes of the tumor under laser irradiation (Figure 5b). After the injection of AMB-1, the temperature of the tumor site rapidly increases under 1064 nm laser irradiation, reaching 48 °C within 5 min. In contrast, the temperature of the tumor injected with PBS only increases to 35 °C. These results confirm that AMB-1 can also effectively convert light into heat within tumor tissues. To further investigate the *in vivo* photothermal therapy performance of AMB-1, we randomly
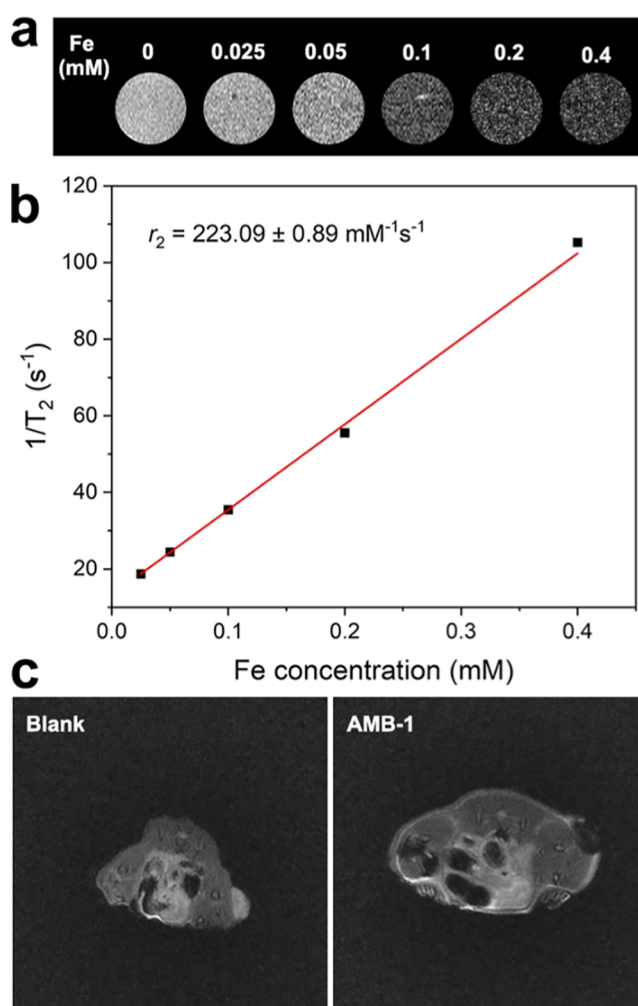
Figure 4. (a) T_2-weighted phantom images and (b) transverse relaxivity measurement fitting plot of AMB-1 at 0.5 T. (c) T_2-weighted images of tumor-bearing mice without and with the injection of AMB-1.

Figure 5. (a) Hypoxia- and lipopolysaccharide-specific stained immunohistochemical tumor sections 2, 5, and 7 mm away from the peritumoral injection point. The red arrows indicate the AMB-1 bacteria. (b) Infrared thermography of tumor-bearing mice after the injection of AMB-1 or PBS under 1064 nm laser irradiation. (c) Representative photographs and (d) tumor growth curves of tumor-bearing mice with different treatments (**$P < 0.01$). (e) H&E and (f) TUNEL stained tumor sections collected from tumor-bearing mice with different treatments.

divided MCF-7 tumor-bearing nude mice into three groups with different treatments. In the group in which the mice were treated with AMB-1 and 1064 nm laser irradiation, the growth of the tumor was significantly inhibited (Figure 5c,5d). In comparison, tumors grow rapidly in other control groups. These results demonstrate that AMB-1 exhibits significant tumor inhibitory effects under 1064 nm laser irradiation. The H&E staining of tumor sections reveals the pycnosis and karyolysis of tumor cells in the AMB-1 + laser group, while tumor cells in other control groups maintain normal morphology (Figure 5e). Moreover, TUNEL staining indicates the occurrence of apoptosis of tumor cells in the AMB-1 + laser group, in which a large amount of green fluorescence can be observed (Figure 5f). These results further confirm that the tumor tissue is seriously burned after the AMB-1-mediated photothermal treatment. We also monitor the biosafety of this treatment. The body weight of the mice showed no significant decrease after all treatments (Figure S6). Meanwhile, H&E staining images collected 10 days after the treatments demonstrate no noticeable damages or inflammatory lesions in the major organs of the mice such as the heart, liver, spleen, lung, and kidney, suggesting the safety of the AMB-1-mediated NIR-II photothermal treatment (Figure S7). It is noteworthy

that the heat generated during the photothermal treatment can also inhibit the growth of AMB-1. SEM images reveal that AMB-1 loses its structural integrity and that the membrane and cytoplasm are ruptured after the photothermal treatment (Figure S8). The inactivation of AMB-1 bacteria after the treatment further ensures the safety of the treatment. Furthermore, the hemolysis assay of AMB-1 indicates that little hemolysis of red blood cells is detected even at the highest concentration, suggesting the high blood compatibility of AMB-1 (Figure S9). In addition, H&E staining shows that AMB-1 does not generate acute toxicity to major organs after intravenous injection (Figure S10).

4. CONCLUSIONS

In summary, we have investigated the intrinsic photothermal performance of magnetotactic bacteria AMB-1 in this work. We demonstrate that AMB-1 has a high NIR-II photothermal conversion efficiency of up to 41.56%, which can efficiently convert the 1064 nm laser into heat. Cell experiments show that AMB-1 can effectively inhibit the proliferation of tumor cells by inducing apoptosis under a 1064 nm laser irradiation. *In vivo* studies reveal that AMB-1 presents a tumor hypoxia-colonizing nature that can actively penetrate the solid tumor and selectively colonize deep tumor hypoxic areas. The efficient penetration and retention of AMB-1 in tumors are beneficial for its *in vivo* photothermal effects, which can mediate tumor heating under 1064 nm laser irradiation for efficient tumor thermal ablation.

■ ASSOCIATED CONTENT

ⓈⒾ Supporting Information

The Supporting Information is available free of charge at https://pubs.acs.org/doi/10.1021/acsomega.4c02914.

> EDX elemental mapping; temperature elevation curves; photothermal performance testing and photothermal conversion efficiency measurement fitting plot of AMB-1 suspension; body weight changes and H&E-stained images of different treatments; and SEM images and hemolysis assay of AMB-1 (PDF)

■ AUTHOR INFORMATION

Corresponding Authors

Liqun Chen − *College of Biological Science and Engineering, Fuzhou University, Fuzhou 350116, P. R. China*; Email: lqchen@fzu.edu.cn

Dengke Hong − *Department of Vascular Surgery, Fujian Medical University Union Hospital, Fuzhou 350001, P. R. China*; Email: dkhong@fjmu.edu.cn

Lihong Chen − *Department of Radiology, Fujian Medical University Union Hospital, Fuzhou 350001, P. R. China*; Email: lihongchen01@fjmu.edu.cn

Authors

Guoming Huang − *College of Biological Science and Engineering, Fuzhou University, Fuzhou 350116, P. R. China*; ⓞ orcid.org/0000-0002-8075-5205

Guifen Zhu − *College of Biological Science and Engineering, Fuzhou University, Fuzhou 350116, P. R. China*

Ruipeng Lin − *College of Biological Science and Engineering, Fuzhou University, Fuzhou 350116, P. R. China*

Wenwen Chen − *College of Biological Science and Engineering, Fuzhou University, Fuzhou 350116, P. R. China*

Rong Chen − *College of Biological Science and Engineering, Fuzhou University, Fuzhou 350116, P. R. China*

Yutong Sun − *College of Biological Science and Engineering, Fuzhou University, Fuzhou 350116, P. R. China*

Complete contact information is available at:
https://pubs.acs.org/10.1021/acsomega.4c02914

Notes

The authors declare no competing financial interest.

■ ACKNOWLEDGMENTS

■ REFERENCES

(1) Li, X.; Lovell, J. F.; Yoon, J.; Chen, X. Clinical development and potential of photothermal and photodynamic therapies for cancer. *Nat. Rev. Clin. Oncol.* **2020**, *17*, 657−674.

(2) Vankayala, R.; Hwang, K. C. Near-Infrared-Light-Activatable Nanomaterial-Mediated Phototheranostic Nanomedicines: An Emerging Paradigm for Cancer Treatment. *Adv. Mater.* **2018**, *30*, No. 1706320.

(3) Hu, J.-J.; Cheng, Y.-J.; Zhang, X.-Z. Recent advances in nanomaterials for enhanced photothermal therapy of tumors. *Nanoscale* **2018**, *10*, 22657−22672.

(4) Aboeleneen, S. B.; Scully, M. A.; Harris, J. C.; Sterin, E. H.; Day, E. S. Membrane-wrapped nanoparticles for photothermal cancer therapy. *Nano Convergence* **2022**, *9*, No. 37.

(5) Guo, T.; Lin, Y.; Jin, G.; Weng, R.; Song, J.; Liu, X.; Huang, G.; Hou, L.; Yang, H. Manganese-phenolic network-coated black phosphorus nanosheets for theranostics combining magnetic resonance/photoacoustic dual-modal imaging and photothermal therapy. *Chem. Commun.* **2019**, *55*, 850−853.

(6) Guo, T.; Tang, Q.; Guo, Y.; Qiu, H.; Dai, J.; Xing, C.; Zhuang, S.; Huang, G. Boron Quantum Dots for Photoacoustic Imaging-Guided Photothermal Therapy. *ACS Appl. Mater. Interfaces* **2021**, *13*, 306−311.

(7) Lin, P.; Luo, P.; Guo, Y.; Qiu, H.; Wang, M.; Huang, G. Tantalum Nitride Nanosheets for Photoacoustic Imaging-Guided Photothermal Cancer Therapy. *Part. Part. Syst. Charact.* **2021**, *38*, No. 2100113.

(8) Rosenblum, D.; Joshi, N.; Tao, W.; Karp, J. M.; Peer, D. Progress and challenges towards targeted delivery of cancer therapeutics. *Nat. Commun.* **2018**, *9*, No. 1410.

(9) Zhao, Z.; Ukidve, A.; Kim, J.; Mitragotri, S. Targeting Strategies for Tissue-Specific Drug Delivery. *Cell* **2020**, *181*, 151−167.

(10) Qian, X.; Xu, X.; Wu, Y.; Wang, J.; Li, J.; Chen, S.; Wen, J.; Li, Y.; Zhang, Z. Strategies of engineering nanomedicines for tumor retention. *J. Controlled Release* **2022**, *346*, 193−211.

(11) Ribatti, D.; Nico, B.; Crivellato, E.; Vacca, A. The structure of the vascular network of tumors. *Cancer Lett.* **2007**, *248*, 18−23.

(12) Munn, L. L.; Jain, R. K. Vascular regulation of antitumor immunity. *Science* **2019**, *365*, 544−545.

(13) Dewhirst, M. W.; Secomb, T. W. Transport of drugs from blood vessels to tumour tissue. *Nat. Rev. Cancer* **2017**, *17*, 738−750.

(14) Cox, T. R. The matrix in cancer. *Nat. Rev. Cancer* **2021**, *21*, 217−238.

(15) Henke, E.; Nandigama, R.; Ergün, S. Extracellular Matrix in the Tumor Microenvironment and Its Impact on Cancer Therapy. *Front. Mol. Biosci.* **2020**, *6*, No. 160.

(16) Jang, S. H.; Wientjes, M. G.; Lu, D.; Au, J. L. S. Drug Delivery and Transport to Solid Tumors. *Pharm. Res.* **2003**, *20*, 1337−1350.

(17) Shen, H.; Aggarwal, N.; Wun, K. S.; Lee, Y. S.; Hwang, I. Y.; Chang, M. W. Engineered microbial systems for advanced drug delivery. *Adv. Drug Delivery Rev.* **2022**, *187*, No. 114364.

(18) Hosseinidoust, Z.; Mostaghaci, B.; Yasa, O.; Park, B. W.; Singh, A. V.; Sitti, M. Bioengineered and biohybrid bacteria-based systems for drug delivery. *Adv. Drug Delivery Rev.* **2016**, *106*, 27−44.

(19) Li, Z.; Wang, Y.; Liu, J.; Rawding, P.; Bu, J.; Hong, S.; Hu, Q. Chemically and Biologically Engineered Bacteria-Based Delivery

Systems for Emerging Diagnosis and Advanced Therapy. *Adv. Mater.* **2021**, *33*, No. 2102580.

(20) Sørensen, B. S.; Horsman, M. R. Tumor Hypoxia: Impact on Radiation Therapy and Molecular Pathways. *Front. Oncol.* **2020**, *10*, No. 562, DOI: 10.3389/fonc.2020.00562.

(21) Vaupel, P.; Mayer, A. Hypoxia in cancer: significance and impact on clinical outcome. *Cancer Metastasis Rev.* **2007**, *26*, 225−239.

(22) Tredan, O.; Galmarini, C. M.; Patel, K.; Tannock, I. F. Drug resistance and the solid tumor microenvironment. *JNCI, J. Natl. Cancer Inst.* **2007**, *99*, 1441−1454.

(23) Wang, L.; Cao, Z.; Zhang, M.; Lin, S.; Liu, J. Spatiotemporally Controllable Distribution of Combination Therapeutics in Solid Tumors by Dually Modified Bacteria. *Adv. Mater.* **2022**, *34*, No. 2106669.

(24) Chen, W.; He, C.; Qiao, N.; Guo, Z.; Hu, S.; Song, Y.; Wang, H.; Zhang, Z.; Ke, B.; Sun, X. Dual drugs decorated bacteria irradiate deep hypoxic tumor and arouse strong immune responses. *Biomaterials* **2022**, *286*, No. 121582.

(25) Sun, R.; Liu, M.; Lu, J.; Chu, B.; Yang, Y.; Song, B.; Wang, H.; He, Y. Bacteria loaded with glucose polymer and photosensitive ICG silicon-nanoparticles for glioblastoma photothermal immunotherapy. *Nat. Commun.* **2022**, *13*, No. 5127.

(26) Chu, B.; Yang, Y.; Tang, J.; Song, B.; He, Y.; Wang, H. Trojan Nanobacteria System for Photothermal Programmable Destruction of Deep Tumor Tissues. *Angew. Chem.* **2022**, *134*, No. e202208422.

(27) Akolpoglu, M. B.; Alapan, Y.; Dogan, N. O.; Baltaci, S. F.; Yasa, O.; Tural, G. A.; Sitti, M. Magnetically steerable bacterial microrobots moving in 3D biological matrices for stimuli-responsive cargo delivery. *Sci. Adv.* **2022**, *8*, No. eabo6163.

(28) Chen, W.; Wang, Y.; Qin, M.; Zhang, X.; Zhang, Z.; Sun, X.; Gu, Z. Bacteria-Driven Hypoxia Targeting for Combined Biotherapy and Photothermal Therapy. *ACS Nano* **2018**, *12*, 5995−6005.

(29) Xing, J.; Yin, T.; Li, S.; Xu, T.; Ma, A.; Chen, Z.; Luo, Y.; Lai, Z.; Lv, Y.; Pan, H.; Liang, R.; Wu, X.; Zheng, M.; Cai, L. Sequential Magneto-Actuated and Optics-Triggered Biomicrorobots for Targeted Cancer Therapy. *Adv. Funct. Mater.* **2021**, *31*, No. 2008262.

(30) Chen, F.; Zang, Z.; Chen, Z.; Cui, L.; Chang, Z.; Ma, A.; Yin, T.; Liang, R.; Han, Y.; Wu, Z.; Zheng, M.; Liu, C.; Cai, L. Nanophotosensitizer-engineered Salmonella bacteria with hypoxia targeting and photothermal-assisted mutual bioaccumulation for solid tumor therapy. *Biomaterials* **2019**, *214*, No. 119226.

(31) Bazylinski, D. A.; Frankel, R. B. Magnetosome formation in prokaryotes. *Nat. Rev. Microbiol.* **2004**, *2*, 217−230.

(32) Faivre, D.; Schuler, D. Magnetotactic bacteria and magnetosomes. *Chem. Rev.* **2008**, *108*, 4875−4898.

(33) Chen, C.; Wang, P.; Chen, H.; Wang, X.; Halgamuge, M. N.; Chen, C.; Song, T. Smart Magnetotactic Bacteria Enable the Inhibition of Neuroblastoma under an Alternating Magnetic Field. *ACS Appl. Mater. Interfaces* **2022**, *14*, 14049−14058.

(34) Chen, X.; Lai, L.; Li, X.; Cheng, X.; Shan, X.; Liu, X.; Chen, L.; Chen, G.; Huang, G. Magnetotactic bacteria AMB-1 with active deep tumor penetrability for magnetic hyperthermia of hypoxic tumors. *Biomater. Sci.* **2022**, *10*, 6510−6516.

(35) Wang, P.; Chen, C.; Wang, Q.; Chen, H.; Chen, C.; Xu, J.; Wang, X.; Song, T. Tumor inhibition via magneto-mechanical oscillation by magnetotactic bacteria under a swing MF. *J. Controlled Release* **2022**, *351*, 941−953.

(36) Lyu, Y.; Li, J.; Pu, K. Second Near-Infrared Absorbing Agents for Photoacoustic Imaging and Photothermal Therapy. *Small Methods* **2019**, *3*, No. 1900553.